RSC Advances

ROYAL SOCIETY OF CHEMISTRY

PAPER

View Article Online
View Journal | View Issue

Check for updates

Cite this: *RSC Adv.*, 2022, **12**, 33239

Dual-mode vehicles with simultaneous thermometry and drug release properties based on hollow Y_2O_3:Er,Yb and $Y_2O_2SO_4$:Er,Yb spheres†

Sonali Mohanty,[ab] Simona Premcheska,[ac] Joost Verduijn,[c] Hannes Rijckaert,[d] Andre G. Skirtach,[c] Kristof Van Hecke[*b] and Anna M. Kaczmarek[*a]

Received 30th September 2022
Accepted 14th November 2022

DOI: 10.1039/d2ra06162g

rsc.li/rsc-advances

Employing luminescence thermometry in the biomedical field is undeniably appealing as many health conditions are accompanied by temperature changes. In this work, we show our ongoing efforts and results at designing novel vehicles for dual-mode thermometry and pH-dependent drug release based on hollow spheres. Hereby for that purpose, we exploit the hollow Y_2O_3 and $Y_2O_2SO_4$ host materials. These two inorganic hollow phosphors were investigated and showed to have excellent upconversion Er^{3+}–Yb^{3+} luminescence properties and could be effectively used as optical temperature sensors in the physiological temperature range when induced by near-infrared CW light (975 nm). Further, doxorubicin was exploited as a model anti-cancer drug to monitor the pH-dependent drug release of these materials showing that they can be used for simultaneous thermometry and drug delivery applications.

Introduction

Health conditions such as cancer, inflammations, heart attacks, and brain seizures lead to hyperlocal temperature changes in the human body.[1,2] Based on this knowledge, we know that temperature measurements are of immense importance for diagnostic purposes, starting from localization, mapping, tracing, and ultimately treatment.[3,4] For applications in biomedicine the temperature range of 20–50 °C is crucial, and is often referred to as the physiological range. For future real-life application in biomedicine, it is important that the measurements are done in a straightforward and non-invasive way to avoid any unnecessary pain and side effects to the patient.[1] To date, techniques such as infrared light (IR) thermography or Raman spectroscopy-based thermometry have been proposed to precisely detect temperature locally and non-invasively.[5] Yet, as a downside, IR cameras provide temperature distributions only of the surface, with estimated thermal emissivity from a short distance. Additional disadvantages of this technique are a large temperature uncertainty and a low spatial resolution. On the one hand, although Raman thermometry can effectively probe the temperature of a system <1 μm in both solids and liquids, it struggles with low signal levels and crosstalk with fluorescent molecules. On the other hand, thermometers based on luminescence detection promise obtaining a high thermal sensitivity ($S_r > 1\%$ per °C), good thermal resolution ($\delta < 0.1$ °C), thermal imaging through the object surface, in many cases high brightness in the infrared biological windows (650–1700 nm) and measuring in the desired physiologically relevant temperature region.[4,6] The development of such luminescence thermometers, and their use in biological systems, could be a solution to important persisting challenges, such as early tumor detection, real-time intra-tumoral *in vitro* or *in vivo* thermal sensing, *in vivo* localized inflammation detection, *etc.*[7,8] In the development of luminescence thermometers, it is also necessary to ensure that the designed materials do not inflict acute toxicity on viable tissue and show good clearance from the body.[3]

Thus far, numerous luminescent materials have already been proposed as luminescent thermometers for potential use in biomedicine *e.g.*, quantum dots (QDs), fluorescent dyes, polymers, lanthanide (Ln)-doped metal–organic frameworks (MOFs), and lanthanide-doped nanoparticles.[9–11] Among them, lanthanide-based materials are proving to be excellent materials for luminescence thermometry, as they have a large number of closely-lying emissive excited energy states originating from the $4f^n$ configuration. This allows luminescence detection in a wide range – from the ultraviolet (UV) over the

---

[a] *NanoSensing Group, Department of Chemistry, Ghent University, Krijgslaan 281-S3, 9000 Ghent, Belgium. E-mail: Kristof.VanHecke@UGent.be; Anna.Kaczmarek@UGent.be*

[b] *XStruct, Department of Chemistry, Ghent University, Krijgslaan 281-S3, 9000 Ghent, Belgium*

[c] *NanoBiotechnology Group, Department of Biotechnology, Faculty of Bioscience Engineering, Ghent University, Proeftuinstraat 86, 9000 Ghent, Belgium*

[d] *SCRiPTS, Department of Chemistry, Ghent University, Krijgslaan 281-S3, 9000 Ghent, Belgium*

† Electronic supplementary information (ESI) available: Detailed synthesis procedure, TG-DTA graphs, additional HAADF-STEM with its EDX maps and additional luminescence spectra. See DOI: **https://doi.org/10.1039/d2ra06162g**

visible to near-infrared (NIR).[12] Upconversion (UC) materials have been studied extensively as they have promising applications in three-dimensional displays, optical, optoelectronic, and chemical sensors, solar cells, biological fluorescence labels and probes, anti-counterfeiting, and other applications.[13,14] An exciting line of research in the nanotheranostic field now exploits UC luminescence which enhances the drug release of certain model drugs *e.g.*, doxorubicin (DOX) from the transporting vessels.[15]

Nonetheless, developing efficiently emitting nanothermometers that fulfill all of these prerequisites for *in vivo* applications is beyond a trivial task. Many reported Ln-based luminescent materials have already shown very good potential for certain biomedical applications, but there are still some significant challenges that need to be resolved, such as obtaining sufficiently high brightness and relative sensitivity, obtaining real-time high spatio-temporal resolution, 3D, reliable, real-time *in vivo* monitoring at a very small temperature step, and the design of active nanothermometers (combined nanocooler/nanoheater-thermometer systems).[16–18] In order to make translational application of these materials, it is important to move towards (nano)theranostics, where the nanothermometers need to show potential to be coupled with a treatment method for a certain targeted disease (*e.g.*, drug delivery, photodynamic therapy, or photothermal therapy).[19,20] And simultaneously these materials need to show low-to-no toxicity toward healthy cells and tissue in the human body.

Inorganic hollow materials with controllable composition and shape are very attractive for various applications due to their superior properties which include low density, large specific surface area, and good permeability.[21–24] Such materials have great potential for applications in drug delivery, but also photodynamic therapy, sensing, cell labeling, waste removal, or catalysis. One of the most intriguing aspects is that hollow materials also allow the development of multifunctional materials, which can combine several functions in one material, *e.g.*, sensing and drug delivery, which is the aim of this work. For the preparation of inorganic hollow materials both a template, as well as a template-free process can be used.[25] As a template often silica, carbon spheres, or polystyrene beads are employed.[26,27] Sacrificial templates, such as rare-earth hydroxyl carbonates can also be used.[25]

In our work, two different inorganic hollow materials were prepared with the notion of combining thermometry (as a diagnostic tool) with drug release in one material. Our synthesis was based on a modified previously reported double-shelled hollow spheres composed of an inner Y_2O_3 shell doped with Yb^{3+} and Er^{3+}, and an outer, mesoporous silica shell.[28] Also, as a second material – yttrium oxysulfate hollow spheres doped with Yb^{3+} and Er^{3+} was prepared, using L-cysteine as the sulfur source, in a hydrothermal synthesis involving the Ostwald ripening process. This synthesis was also based on a previously reported route.[29]

Ln^{3+}-doped Y_2O_3 has widely been studied as an upconversion material due to its high thermal stability, chemical durability, relatively low phonon energy, and low thermal expansion of yttrium oxide. In Y_2O_3:Er,Yb the ratio of the green-to-red emission can easily be tuned by changing the Yb^{3+} sensitizer concentration, as has been reported previously in literature.[30]

Rare-earth oxysulfate ($RE_2O_2SO_4$) materials are important matrix compounds for luminescent materials and have attracted quite some attention in recent years, due to their specific magnetic properties, large oxygen storage volume, and unique luminescent properties.[31,32] The $RE_2O_2SO_4$ material has already shown to be an excellent host for upconversion applications, which is why it was selected for this study alongside the Y_2O_3 material.[33,34] This material has ideal chemical and thermal stability as well as a high size and shape tunability. Many types of synthetic approaches can be used including single precursor decomposition, urea-based aqueous synthesis, molten salt synthesis, combustion synthesis, and others.[34] $RE_2O_2SO_4$ shows very good structural stability when replacing Y^{3+} ions with other rare-earth metal ions, which is very important for designing materials with a high doping percentage of emissive lanthanide ions. Two different rare-earth ions can easily be co-doped into the crystal structure of the material in optimal ratios without modifying the host structure or significantly changing the lattice constant. This particular oxysulfate has also not been explored much for thermometry or drug release; therefore, it was of interest for our investigation.

In this work, we investigated both Y_2O_3:Er,Yb and $Y_2O_2SO_4$:Er,Yb hollow spheres for potential applications such as luminescence thermometers and drug carriers, employing DOX as a model anticancer drug.

Results and discussion

A schematic overview of the development of Y_2O_3:Er,Yb hollow spheres is presented in Scheme 1. The synthesis of double-shelled Y_2O_3:Er,Yb is complex and had to be carried out in several steps based on a previously reported synthesis route.[28] The detailed synthesis route of the material is presented in the Experimental section. Briefly, carbon nanoparticles (CNPs) of 200–400 nm in size were prepared *via* a hydrothermal synthesis route. Next, a shell of $Y(OH)CO_3$:Er,Yb was grown around the CNPs template. The CNPs@$Y(OH)CO_3$:Er,Yb particles were then coated with a layer of SiO_2 and after drying the CNPs@$Y(OH)CO_3$:Er,Yb@SiO_2 product was heat-treated at 800 °C to obtain hollow Y_2O_3:Er,Yb spheres. On the contrary, the preparation of $Y_2O_2SO_4$:Er,Yb hollow spheres was simpler undergoing only two synthetic steps, and was also based on a previous report.[29] The precursor material was obtained through a hydrothermal synthesis where L-cysteine and PVP (polyvinylpyrrolidone) were used.[29] To obtain $Y_2O_2SO_4$:Er,Yb hollow spheres the precursor material was heat-treated at 850 °C. All developed materials, obtained at different synthetic stages, were characterized by scanning transmission electron microscopy (STEM) with bright field (BF-STEM) and high-angle annular dark-field detector (HAADF-STEM), and energy dispersive X-ray (EDX) mapping, as well as by scanning electron microscopy (SEM) to monitor the morphology of the obtained materials. The Y_2O_3:Er,Yb, and $Y_2O_2SO_4$:Er,Yb materials (for $Y_2O_2SO_4$ both the $Y_2O_2SO_4$:Er,Yb precursor and $Y_2O_2SO_4$:Er,Yb heat treated (HT) materials were investigated) were characterized by powder XRD and nitrogen

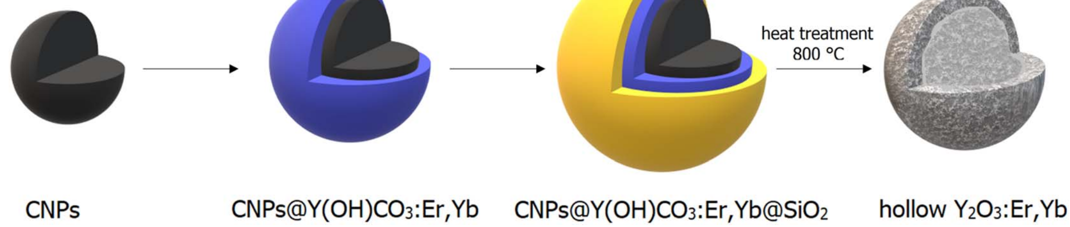

Scheme 1 Schematic overview of the preparation of Y_2O_3:Er,Yb hollow spheres, starting from carbon nanoparticles (CNPs). A shell of Y(OH)CO_3:Er,Yb was first grown around the CNPs, which were then coated with a layer of SiO_2 and subsequently heat-treated to obtain Y_2O_3:Er,Yb hollow spheres.

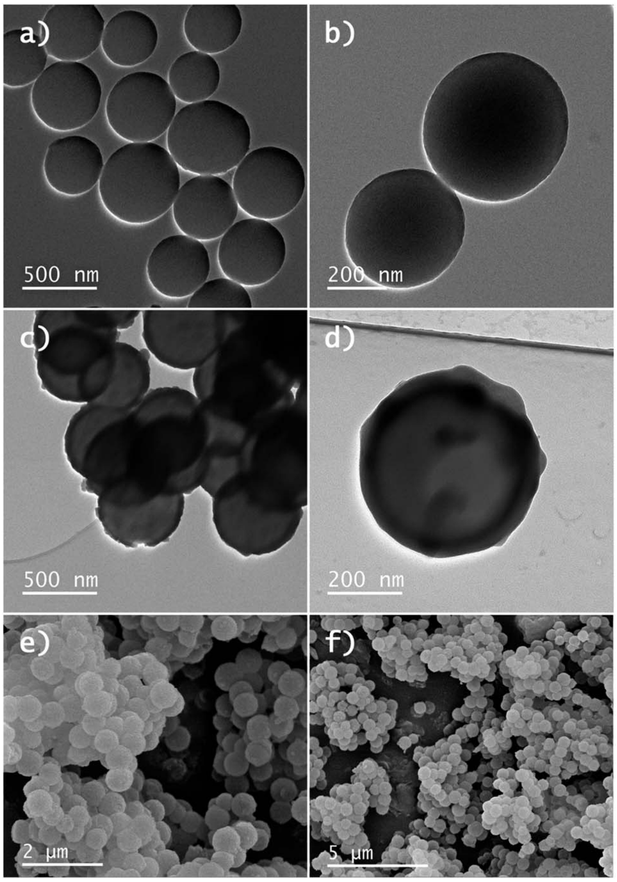

Fig. 1 BF-STEM images of (a) and (b) CNPs obtained in the hydrothermal synthesis and (c) and (d) CNPs@Y(OH)CO_3:Er,Yb spheres and (e) and (f) SEM images of CNPs@Y(OH)CO_3:Er,Yb spheres.

sorption as well as TGA. In Fig. 1 the BF-STEM and SEM images of CNPs (Fig. 1a and b), as well as CNPs@Y(OH)CO_3:Er,Yb (Fig. 1c–f) are presented. The CNPs are around 200–400 nm in size, with uniform size distribution. After growing Y(OH)CO_3:Er,Yb on the CNPs the size of the spherical particles slightly increases, and rough edges of the Y(OH)CO_3:Er,Yb layer are observed. It is clear from the BF-STEM images that the Y(OH)CO_3:Er,Yb layer is distributed on all CNPs. SEM images confirm uniform shapes and sizes of the CNPs@Y(OH)CO_3:Er,Yb material. In Fig. 2, BF-STEM images of the particles after SiO_2 coating and heat-treatment are shown. Hollow Y_2O_3:Er,Yb spheres of 200–400 nm in size are formed. EDX maps confirm the presence of the SiO_2 shell, as well as even distribution of the Er^{3+} and Yb^{3+} dopants in the Y_2O_3 matrix (Fig. 3).

In Fig. 4 the BF-STEM images of the $Y_2O_2SO_4$:Er,Yb precursor and $Y_2O_2SO_4$:Er,Yb HT (after heat-treatment) are presented. For both the precursor (Fig. 4a and b) as well as the $Y_2O_2SO_4$:Er,Yb HT material spherical, urchin-like morphology is obtained. The obtained particles are around 150–200 nm in size, with uniform size distribution. The spheres are hollow even before heat-treatment, without any sufficient changes in morphology (Fig. 4c). Also, for this material, EDX maps confirm an even distribution of the Er^{3+} and Yb^{3+} dopant ions in the $Y_2O_2SO_4$ host matrix (Fig. 5).

The powder XRD patterns (Fig. 6a) of the Y_2O_3:Er,Yb, $Y_2O_2SO_4$:Er,Yb precursor and $Y_2O_2SO_4$:Er,Yb HT materials are presented in Fig. 6a. For Y_2O_3:Er,Yb, characteristic peaks, which can be assigned to the cubic-phase Y_2O_3 (JCPDS card No. 43-0661), are clearly observed. The width of the diffraction peaks for the $Y_2O_2SO_4$:Er,Yb precursor, in the range from about 20° to 60°, suggests that the precursor has some crystallinity, however, the obtained diffraction pattern is inconsistent with any reported data in the JCPDS card database. After being heat treated at 850 °C for 3 hours in air, it is apparent that the crystallinity of the final product has significantly enhanced. XRD analysis shows that this calcined product is mainly composed of $Y_2O_2SO_4$ monoclinic phase (JCPDS 53-0168) with traces of the Y_2O_3 phase as impurity.[30] N_2 sorption measurements were performed on the Y_2O_3:Er,Yb, and $Y_2O_2SO_4$:Er,Yb precursor (Fig. 6b). The BET surface area values of the materials were calculated to be 447 $m^2\ g^{-1}$ and 202 $m^2\ g^{-1}$, for the Y_2O_3:Er,Yb and $Y_2O_2SO_4$:Er,Yb precursor, respectively. We have focused here only on the $Y_2O_2SO_4$:Er,Yb precursor because we have shown that the upconversion properties of this material are more appealing for thermometry applications compared to those of the heat-treated form.

The porous nature of the spheres with hollow cavities makes them ideal for further drug delivery investigations.[34,35]

Thermogravimetric (TG) and Differential Thermal (DTA) analyses were done to determine the thermal stability of the materials. TG-DTA curves for both the Y_2O_3:Er,Yb material and $Y_2O_2SO_4$:Er,Yb precursor were conducted from room temperature to 1000 °C in air, and the obtained TG-DTA curves by

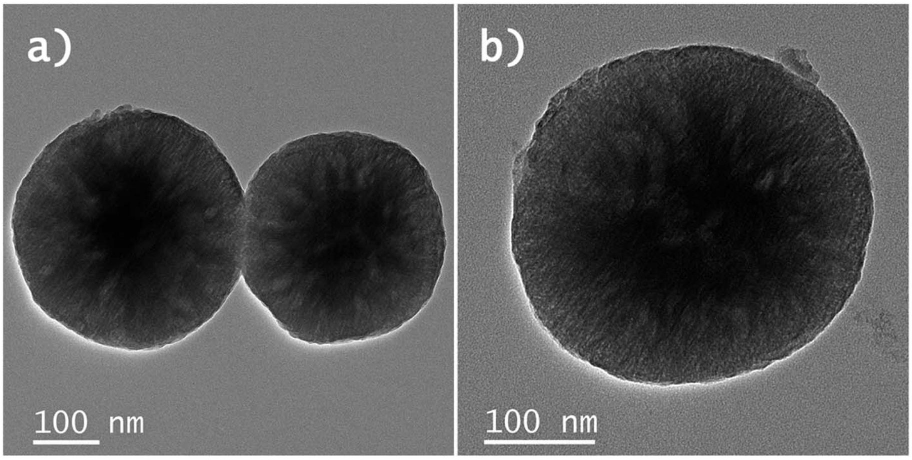

Fig. 2 (a) and (b) BF-STEM images of Y_2O_3:Er,Yb hollow spheres obtained after heat-treatment in air.

a thermal analyzer are shown in Fig. S1 and S2 in the ESI.† For both materials, the initial weight loss before 100 °C is assigned to the removal of the absorbed H_2O. For Y_2O_3 (Fig. S1†), the two rapid weight loss steps can be assigned to the dehydration and subsequent burning of any remainings of the CNP templates, respectively. The maximum mass loss occurs at about 400 °C, which may be attributed to the conversion from the amorphous $Y(OH)CO_3$ precursor to the crystalline Y_2O_3. Furthermore, the DTA curve analysis reveals that all reactions are endothermic. As seen in Fig. S2,† the precursor decomposes completely up to around 550 °C. The exothermic peak on the DTA curve centered at 500 °C and 580 °C indicates that the above process is an exothermic reaction caused by the crystallization of $Y_2O_2SO_4$. However, the weight loss starting at 950 °C is attributed to the decomposition of the $SO_4{}^{2-}$ groups in $Y_2O_2SO_4$, corresponding to the following reaction equation:

$$Y_2O_2SO_4 \rightarrow Y_2O_3 + SO_2\uparrow + \frac{1}{2}O_2\uparrow$$

The luminescence properties of the developed Y_2O_3:Er,Yb, $Y_2O_2SO_4$:Er,Yb precursor and $Y_2O_2SO_4$:Er,Yb HT hollow spheres were studied at room temperature as well as at varying temperatures upon excitation with a 975 nm continuous wave (CW) laser in powder and in aqueous suspensions. The temperature-dependent emission spectra (288.15–328.15 K; 15–

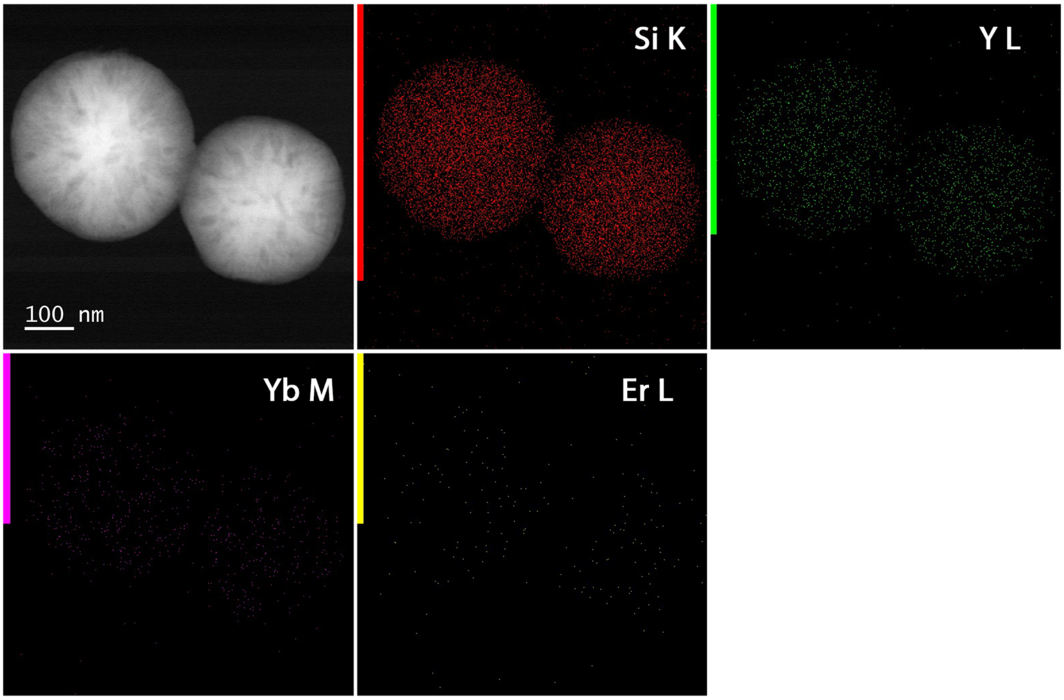

Fig. 3 HAADF-STEM with EDX maps of Y_2O_3:Er,Yb hollow spheres. Si, Y, Yb, and Er were mapped.

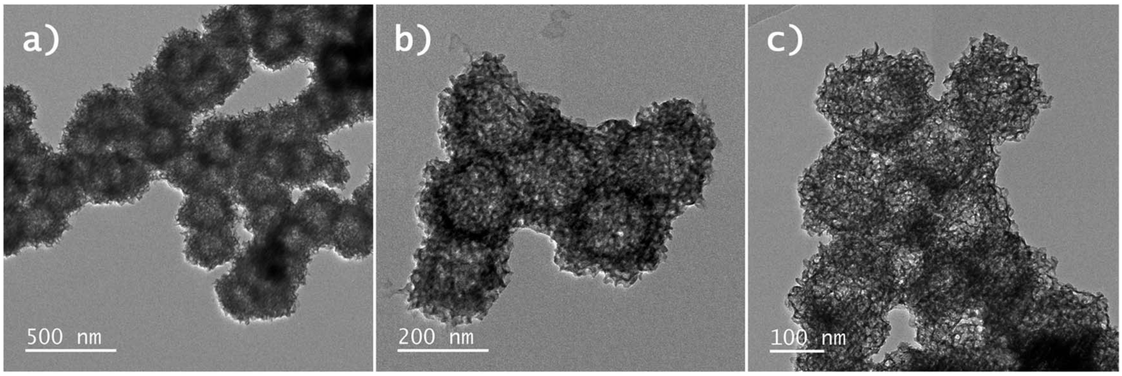

Fig. 4 BF-STEM images of (a) and (b) $Y_2O_2SO_4$:Er,Yb precursor and (c) $Y_2O_2SO_4$:Er,Yb hollow spheres obtained after heat-treatment in air.

55 °C) of Y_2O_3:Er,Yb are presented in Fig. 7. The RT emission of solid Y_2O_3:Er,Yb particles is presented in Fig. S3.† Upon 975 nm laser excitation, strong green upconversion emission due to the $^2H_{11/2} \rightarrow {}^4I_{15/2}$ (522 nm) and $^4S_{3/2} \rightarrow {}^4I_{15/2}$ (563 nm) transitions of Er^{3+} is observed.[36] And even stronger red emission, due to the $^4F_{9/2} \rightarrow {}^4I_{15/2}$ (661 nm) transition can also be observed. The green-to-red emission in the Y_2O_3 host matrix can be tuned by changing the Er^{3+} and Yb^{3+} doping amounts as has previously been described in literature.[30] As NIR luminescence thermometers based on the $^2H_{11/2}$, $^4S_{3/2} \rightarrow {}^4I_{13/2}$ transitions between 790 and 850 nm have previously been reported, we have also investigated the NIR region, however, this material did not show the $^2H_{11/2}$, $^4S_{3/2} \rightarrow {}^4I_{13/2}$ transitions.[36] After dispersing the hollow spheres in distilled water, the thermometric properties of the Y_2O_3:Er,Yb were determined (Fig. 7). Only the green emission region was monitored since we find the peaks relevant for thermometry (as they are thermally coupled levels that can be used for temperature sensing).

The experimental Δ parameter (eqn (1)) was calculated based on the integrated areas under the peaks and was well-fitted using eqn (2).[37,38]

$$\Delta = \frac{I_1}{I_2} \tag{1}$$

$$\Delta = \alpha \exp\left(-\frac{\Delta E}{k_B T}\right) \tag{2}$$

where I_1 and I_2 are the maximum intensities of peaks at the selected wavelengths, and the pre-factor $\alpha = C\,g_2/g_1$. C contains information about the ratio of the radiative transition probabilities from the two thermally coupled levels to the addressed ground level, while g_2 and g_1 are the $(2J+1)$-fold degeneracies of

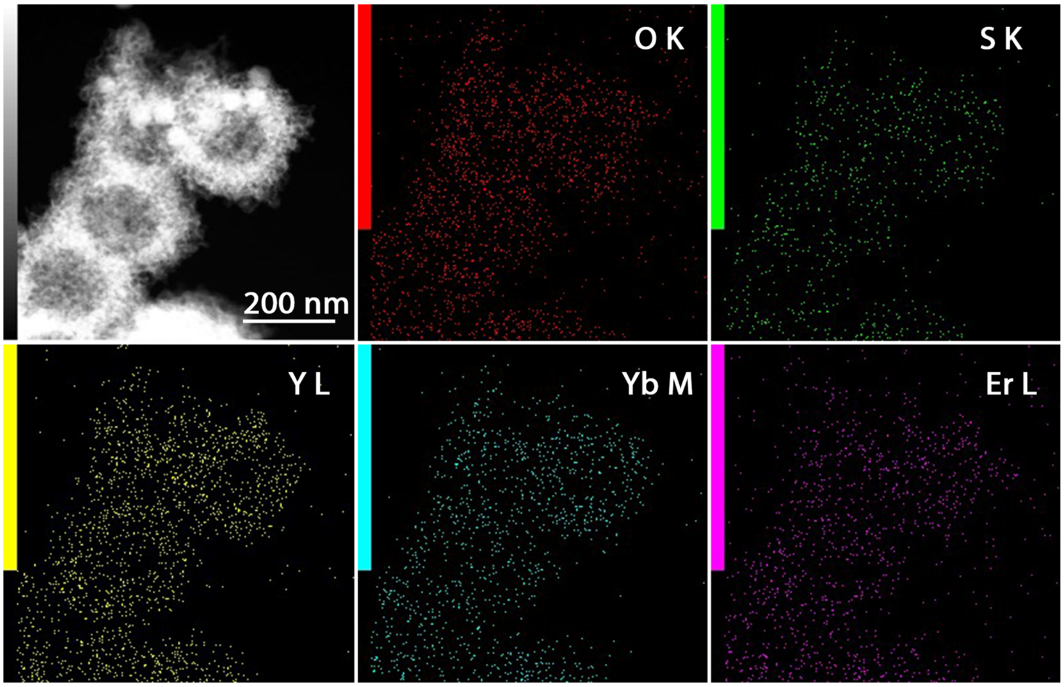

Fig. 5 HAADF-STEM with EDX maps of $Y_2O_2SO_4$:Er,Yb hollow spheres. O, S, Y, Yb, and Er were mapped.

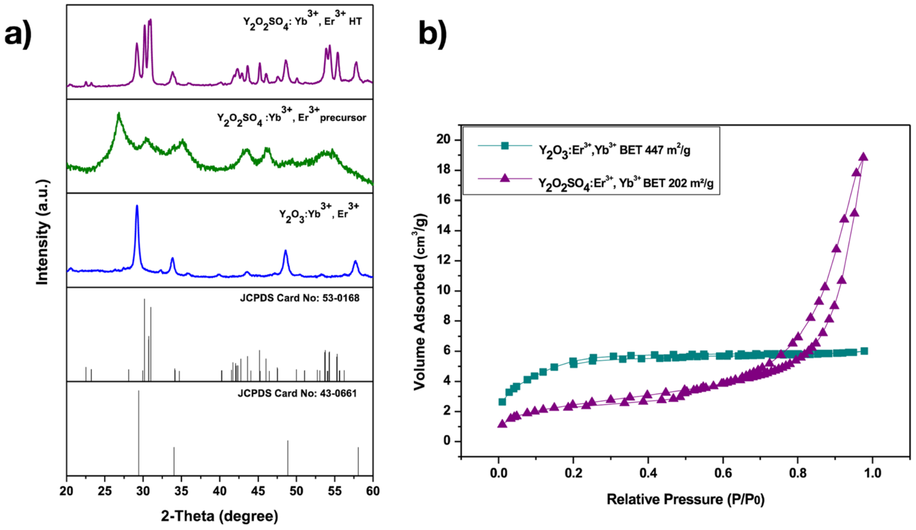

Fig. 6 (a) Powder XRD patterns of Y_2O_3:Er,Yb, and $Y_2O_2SO_4$:Er,Yb (before "precursor" and after heat treatment "HT" at 850 °C for 3 h), (b) N_2 sorption isotherms for Y_2O_3:Er,Yb, and $Y_2O_2SO_4$:Er,Yb precursor.

the thermally coupled levels, and ΔE is the effective energy gap between the two excited levels. The experimentally determined intensity ratios between luminescence from the $^2H_{11/2}$ and $^4S_{3/2}$ levels, respectively, were fitted using eqn (1) to obtain $\Delta E = (633 \pm 32)$ cm^{-1} ($R^2 = 0.991$), which is in good agreement to the values found in literature for this energy gap (700 to 800 cm^{-1} typically found in oxide and fluoride host matrixes).[38] Relative sensitivity S_r (eqn (3)) gives information about the relative change of the thermometric parameter per unit temperature change (in % K^{-1}) and it is independent of the operational principle of the thermometer. It, therefore, allows direct and quantitative comparison of different thermometric materials.[39]

$$S_r = 100\% \times \left|\frac{1}{\Delta}\frac{\partial \Delta}{\partial T}\right| \quad (3)$$

The maximum S_r for the Y_2O_3:Er,Yb material was calculated to be 1.097 % K^{-1} at 288.15 K (Fig. 7). The temperature

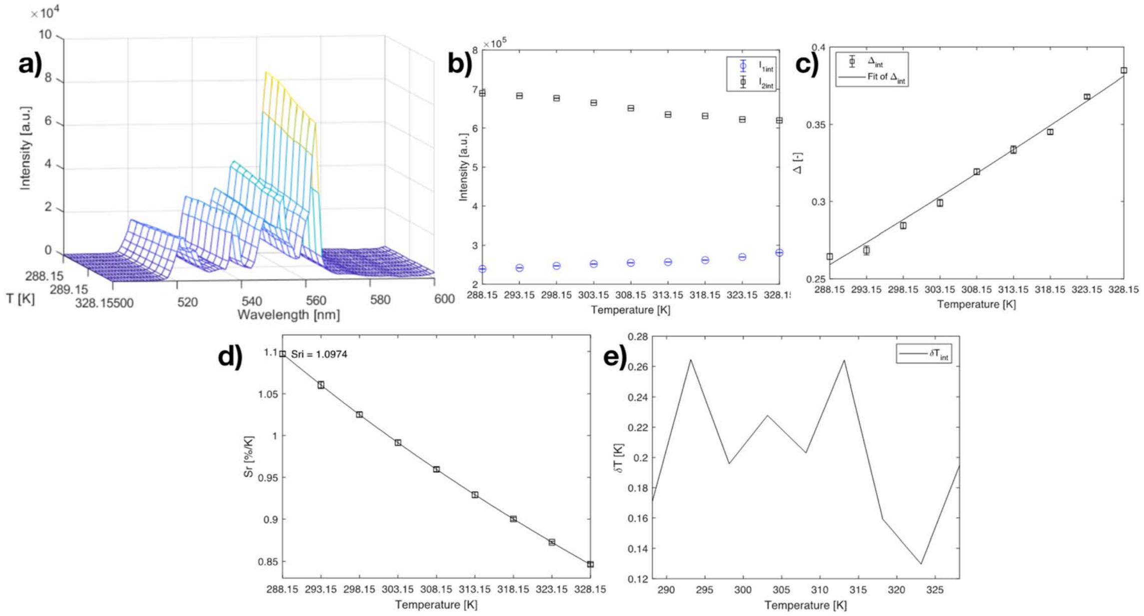

Fig. 7 (a) Emission map of Y_2O_3:Er,Yb at varying temperatures (288.15–328.15 K; step 5 K), (b) intensities of the 522 nm and 563 nm peaks at varying temperatures, (c) calibration curve plot for the Y_2O_3:Er,Yb material using eqn (2) when the 522 nm and 563 nm peaks are considered. The points are experimental Δ parameters, the solid line shows the least-squares fit to the experimental points. (d) relative sensitivity S_r plot at varying temperatures (288.15–328.15 K) for I_{522}/I_{563} ratio, the solid lines are a guide for the eyes. (e) temperature uncertainty graph over the monitored temperature range.

uncertainty (δT) is however the most important parameter to assess the performance of a thermometer (eqn (4)) since it not only includes the relative sensitivity but also the measurement error of the intensity ratio ($\delta\Delta$).

$$\delta T = \frac{1}{S_r}\frac{\delta\Delta}{\Delta} \tag{4}$$

Here, for the Y_2O_3:Er,Yb material, the $\delta T < 0.27$ K throughout the whole temperature range.

Next, the temperature-dependent emission spectra (288.15–328.15 K; 15–55 °C) of the $Y_2O_2SO_4$:Er,Yb precursor are presented in Fig. 8. The precursor was selected for thermometric measurements and not the $Y_2O_2SO_4$:Er,Yb heat-treated material as would be expected, on the account that after heat treatment the green emission necessary for thermometry applications becomes weak compared to the red emission of the material. The RT emission of solid $Y_2O_2SO_4$:Er,Yb particles after heat treatment is presented in Fig. S4.† Upon dispersing in distilled water, the green emission even further decreases (Fig. S5†) and makes it not suitable for a thermometer material.

Here, the NIR $^2H_{11/2}$, $^4S_{3/2} \rightarrow {}^4I_{13/2}$ transitions were visible, however, did not show significant temperature change in the physiological range. For the $Y_2O_2SO_4$:Er,Yb precursor the experimentally determined intensity ratios between the luminescence emissions from the $^2H_{11/2}$ and $^4S_{3/2}$ levels, respectively, were fitted to the model of eqn (1) to obtain $\Delta E = (631 \pm 27)$ cm^{-1} ($R^2 = 0.994$), which is close to the values found in literature for fluoride host materials. The maximum S_r for the $Y_2O_2SO_4$:Er,Yb precursor material was calculated to be 1.095 % K^{-1} at 288.15 K (Fig. 8), which is very similar to that of the Y_2O_3:Er,Yb material. The $\delta T < 0.12$ K throughout the whole temperature range, showing even better results than for the Y_2O_3:Er,Yb material.

Based on these results it can be concluded that both the Y_2O_3:Er,Yb and $Y_2O_2SO_4$:Er,Yb precursor could work well as a physiological thermometer in an aqueous environment. As a proof of principle, on the surface of the $Y_2O_2SO_4$ precursor additionally gold nanoparticles (AuNPs) were grown *in situ* (Fig. 9), to potentially use the AuNPs as nano-heaters for the purposes of developing localized hyperthermia or enhancing the rate of drug release.[40] We have used such a method previously for other materials like hybrid $NaYF_4$:Er,Yb nano-MOF composites and it can be well translated to purely inorganic materials such as the $Y_2O_2SO_4$ shown here.[41] The applications of these materials were not further explored in the work, the objective was to just show the possibilities from a materials point of view.

To further assess their potential use in real biological systems, the cytotoxicity of these materials was tested employing a PrestoBlue™ cell viability assay on *in vitro* cultured human cells *via* fluorescence spectroscopy.[41] Simultaneously, widefield microscopy was exploited to visualize the sample-treated, dye-marked cells applying a Green Fluorescent Protein (GFP) long-pass filter. Here, Normal Human Dermal Fibroblasts (NHDF) were seeded at early passage stages when their growth reached 80–90% confluency. The toxicity of the three materials (Y_2O_3:Er,Yb, $Y_2O_2SO_4$:Er,Yb precursor, as well as the $Y_2O_2SO_4$:Er,Yb@AuNPs) was tested in a concentration-dependent manner on five technical replicates per tested concentration per sample, and the results are presented in Fig. 10. The cell

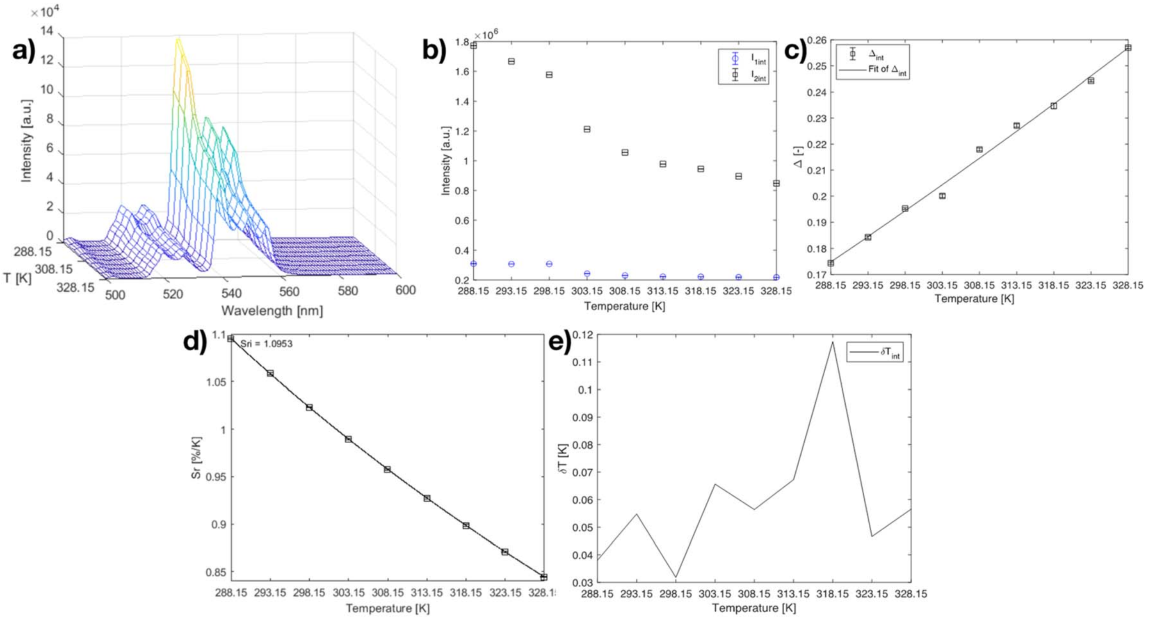

Fig. 8 a) Emission map of $Y_2O_2SO_4$:Er,Yb precursor at varying temperatures (288.15–328.15 K; step 5 K), (b) intensities of the 520 nm and 540 nm peaks at varying temperatures, (c) calibration curve plot for the $Y_2O_2SO_4$:Er,Yb precursor material using eqn (2) when the 520 nm and 540 nm peaks are considered. The points are experimental Δ parameters, and the solid line shows the least-squares fit to the experimental points. (d) relative sensitivity S_r plot at varying temperatures (288.15–328.15 K) for I_{520}/I_{540} ratio, the solid lines are a guide for the eyes. (e) temperature uncertainty graph over the monitored temperature range.

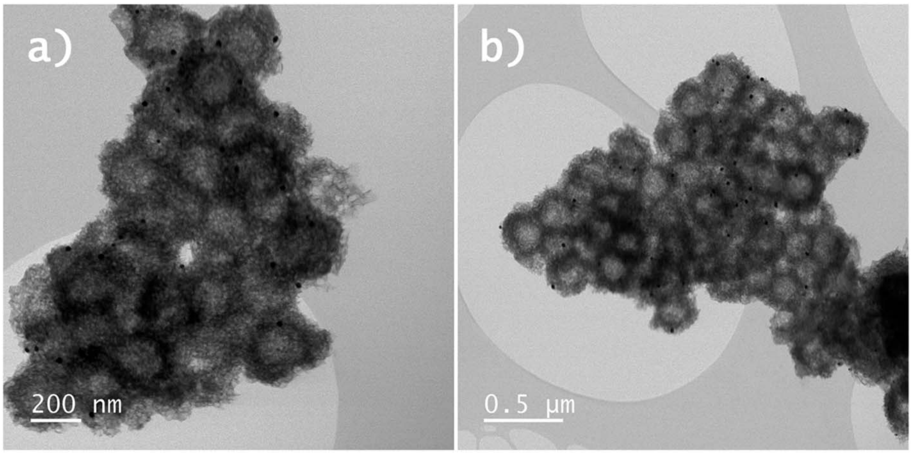

Fig. 9 (a) and (b) BF-STEM images $Y_2O_2SO_4$:Er,Yb@AuNPs precursors hollow spheres. The AuNPs can be observed as small black dots on the surface of the $Y_2O_2SO_4$:Er,Yb@AuNPs hollow spheres.

viability tests indicate that the aforementioned materials are relatively non-toxic in a wide concentration range. The Y_2O_3:Er,Yb compound exhibits a relatively non-toxic trend over the entire investigated concentration range and is therefore deemed generally compatible with the NHDFs. For the $Y_2O_2SO_4$:Er,Yb precursor material, significant toxicity towards fibroblastic cells occurred at a concentration of 1 mg per well or 5.556 mg mL^{-1}, which is a quite high concentration of this compound compared to other similar studies.[42,43] However, when AuNPs are additionally incorporated within the precursor matrix $Y_2O_2SO_4$:Er,Yb, the compound manifests a notable cytotoxic effect, *i.e.*, the cell viability is drastically decreased and varies in a range from 0–25% already at a tested concentration of 0.05 mg per well or 0.278 mg mL^{-1} of the compound. This result is also strengthened by the widefield microscopy imaging as the spindle-shaped cells are no longer discernible in the range of 2.778–5.556 mg mL^{-1} for $Y_2O_2SO_4$:Er,Yb and 0.278–5.556 mg mL^{-1} for $Y_2O_2SO_4$:Er,Yb@AuNPs, respectively. However, as with the pure precursor material, such high concentrations would be futile for biomedical applications, so the current finding does not pose a major concern for further investigations of these materials in the appropriate, optimal dose.[44] What is noteworthy to highlight is how well the cytotoxicity data and the widefield microscopy images complement each other within different technical replicates of the same sample concentrations. This is a preliminary observation of the potentially low replicate variability and good technical reproducibility of the sample measurements.

Due to the hollow nature of the materials, large surface area, non-toxicity to the chosen *in vitro* cultured healthy human cells, and good thermometric properties in water, these materials were further considered to be employed as vehicles for dual-mode activity: combined thermometry and drug release. The materials ($Y_2O_2SO_4$ precursor and Y_2O_3) were in a subsequent step loaded with doxorubicin – a well-explored model drug used in clinical chemotherapy. First, the drug uptake and then the pH-dependent drug release was studied.

For determination of the drug loading efficiency and the drug release behavior of the rare-earth hollow spheres – Y_2O_3:Er,Yb and $Y_2O_2SO_4$:Er,Yb, doxorubicin hydrochloride was chosen as a fluorescent anti-cancer model drug. Because of their large specific surface area and good permeability, both Y_2O_3 and $Y_2O_2SO_4$ can store a relatively large amount of DOX molecules. To quantitatively analyze the uptake of DOX during the experiment, a calibration curve of DOX was drawn using a series of solutions with different concentrations of DOX, *versus* their absorbance at 480 nm. After the sample was loaded with DOX, we evaluated both the drug Loading Capacity (LC%) (eqn S(1) in the ESI†) and the Encapsulation Efficiency (EE%) (eqn S(2) in the ESI†) using both the calibration curve and the measured absorbance value. The LC% of DOX into Y_2O_3:Er,Yb and $Y_2O_2SO_4$:Er,Yb hollow spheres was determined to be 37.0% and 38.3%, respectively. The EE% was found to be 58.6% for Y_2O_3:Er,Yb and 62.0% for $Y_2O_2SO_4$:Er,Yb.

Drug release depending on the pH change of the environment has been extensively studied, as the pH values of cytoplasm, lysosomes, and endosomes vary from 7.2–7.4, 4.5–6.5, and 5.5–6.6, respectively.[44,45] Furthermore, it is known that cancer cells in cancerous tissue have a more acidic pH than in healthy tissue. pH-controlled drug delivery, based on this feature, can be an alternative approach for cancer therapy.

It has previously been reported that DOX drug release from hollow nanoparticles can be enhanced in a more acidic environment.[45] Hence it was suggested that DOX molecules might be released faster in mildly acidic tumor areas than in physiological blood environment in vascular compartments.

Therefore, to explore the pH-responsive behavior of both Y_2O_3:Er,Yb and $Y_2O_2SO_4$:Er,Yb, we have determined the absorbance at 480 nm as a function of time at pH 7.4, pH 5.5 and pH 4 in PBS buffer at 37 °C (corresponding calibration curves for PBS buffer at pH 7.4, pH 5.5 and pH 4 can be found in Fig. S8–S10 in the ESI†). A schematic overview of the DOX loading and release process is presented in Scheme 2. In our experiment, the drug release for both materials was studied for a period of 72 h. The concentration of DOX molecules in the solutions upon release

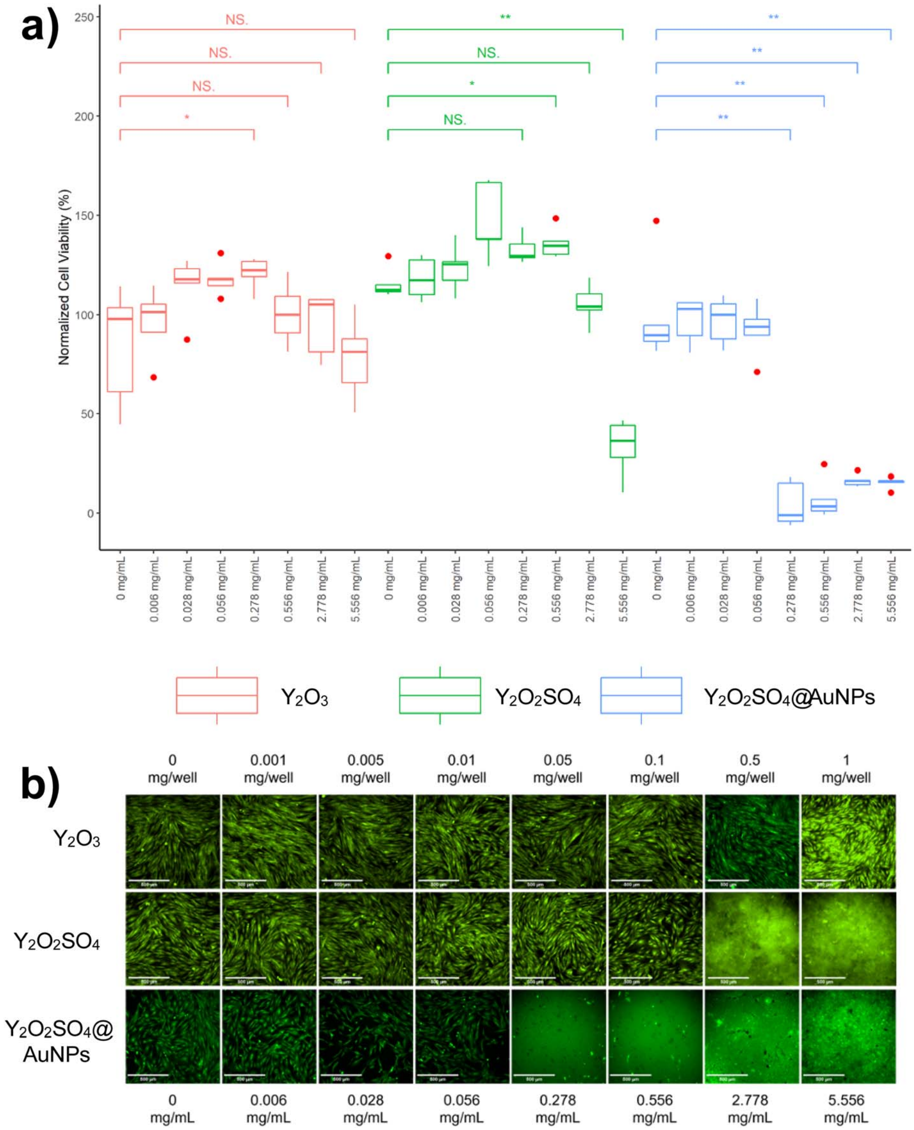

Fig. 10 (a) Boxplot of cytotoxicity test results obtained upon testing the three materials at different concentrations of the three different samples (Y_2O_3:Er,Yb, $Y_2O_2SO_4$:Er,Yb precursor, and $Y_2O_2SO_4$:Er,Yb@AuNPs). Statistical analysis was done applying the Wilcoxon test where, * represents $p < 0.05$, and ** represents $p < 0.01$. (b) Widefield fluorescence microscopy replicates at different concentrations (0, 0.001, 0.005, 0.01, 0.05, 0.1, 0.5, 1 mg per well or 0, 0.006, 0.028, 0.056, 0.278, 0.556, 2.778, 5.556 mg mL^{-1} respectively) of the three different materials (Y_2O_3:Er,Yb, $Y_2O_2SO_4$:Er,Yb precursor, and $Y_2O_2SO_4$:Er,Yb@AuNPs). Cells are stained with Calcein AM green-fluorescent dye visually indicating the degree of cell viability. The scale bars are all set to 500 μm.

was determined using UV-Vis measurements performed at different time intervals.

For Y_2O_3:Er,Yb, about 9% of DOX was released in the neutral condition at pH 7.4, while ∼16% of DOX was released in the acidic PBS solution at pH 5.5 and around 22% DOX was released at pH 4, within 72 h. Whereas, in a neutral pH 7.4 PBS solution, $Y_2O_2SO_4$:Er,Yb released approximately 6% of DOX, around 12% in an acidic pH 5 PBS solution, and nearly 26% in a pH 4 PBS solution within 72 h (Fig. 11). Table S1 in the ESI† summarizes the DOX loading and release results for both materials. It is clear from these results that our materials take up DOX very well and release it gradually with clear pH dependency.

To date, not much work has been done on combining thermometry with drug delivery. However, there are quite some reports on (hollow) inorganic particles for DOX release that can be used as a reference for comparison with our drug loading and release results. For example, Yi *et al.* reported $GdPO_4$:Ce,Tb hollow spheres for the loading and release of doxorubicin. They showed that when the pH was 5, 47% of the loaded DOX was released in just 10 hours, whereas at pH 7.4, only 30% of the drug was released showing pH-dependent release of this inorganic host. However, drug loading efficiency was only 17%, which is much lower than that of our materials.[46] Moreover, Huang *et al.* reported that the DOX loading efficiency of the $(PAH/PSS)_2@Gd_2O_3:Yb^{3+}$, Er^{3+}@MSNs was only 10.3%. with

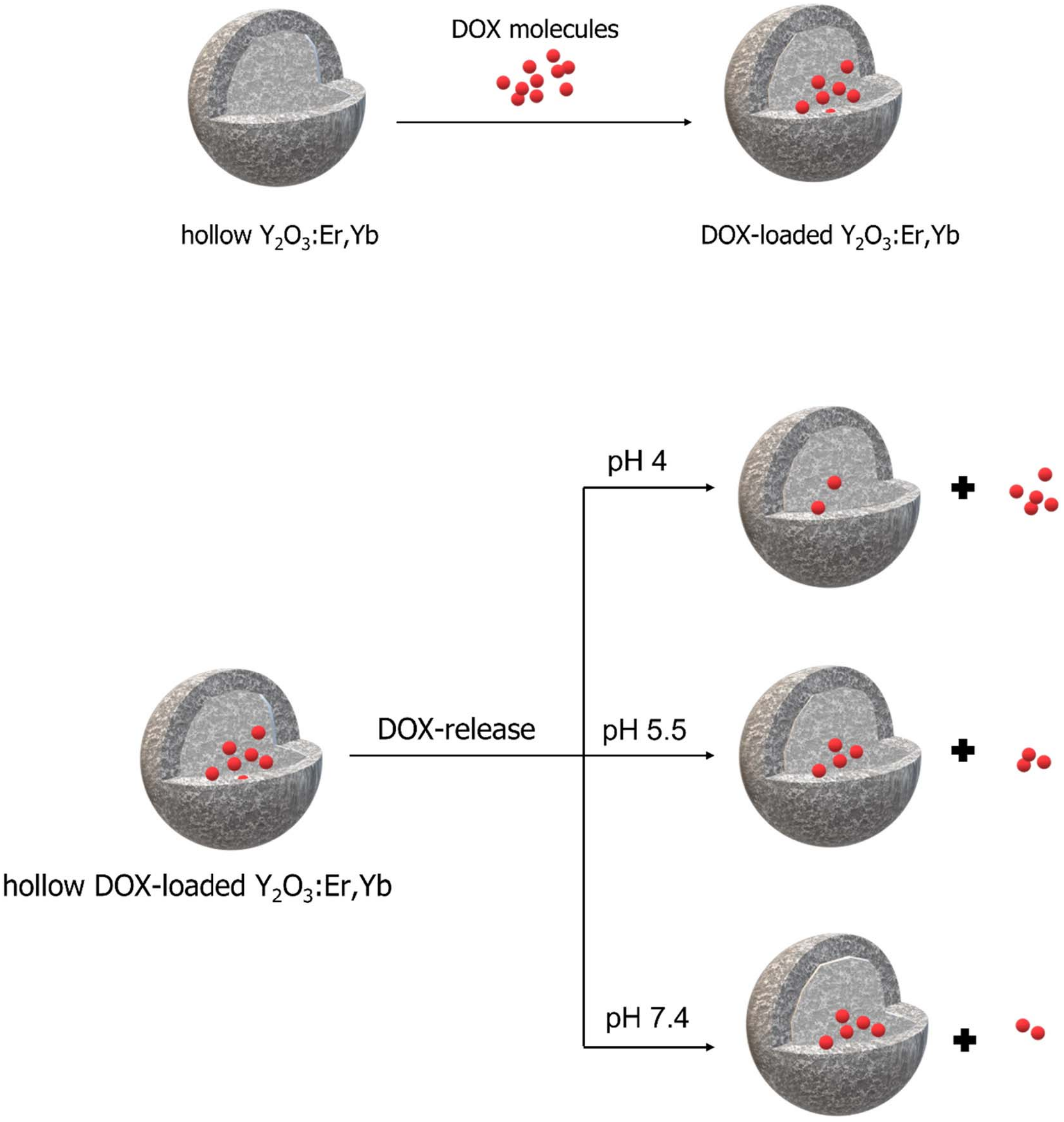

Scheme 2 Schematic overview of the DOX loading (top) and release process at different pH values (bottom) using Y_2O_3:Er,Yb as example.

9.4% of the DOX being released at pH 7.4 after 72 hours and a faster release profile of roughly 64% over the same period of time at pH 5.2. The fast release of this material can be attributed to the diffusion of DOX loaded in the polymer shell and the outer surface of the silica nanoparticles.[47] Ge *et al.* studied the release pattern of DOX from the hollow Y_2O_3:Yb^{3+},Er^{3+} sphere in

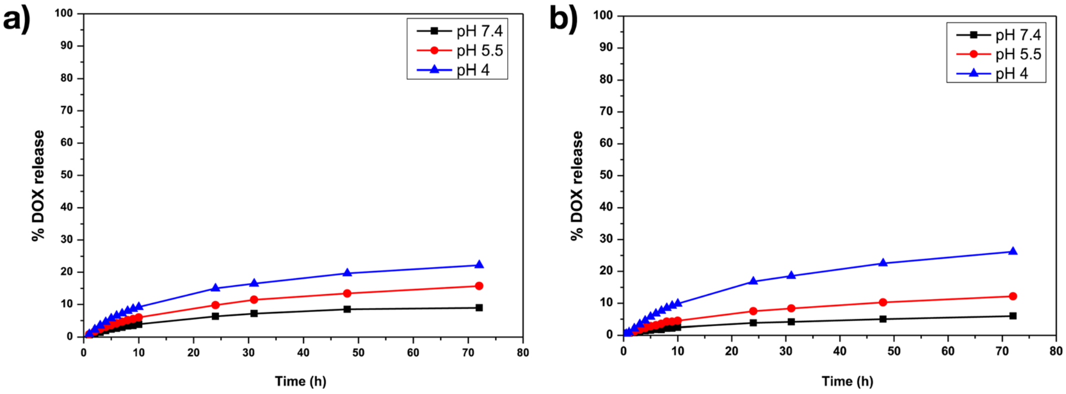

Fig. 11 DOX drug release profiles for (a) Y_2O_3:Er,Yb-DOX, (b) $Y_2O_2SO_4$:Er,Yb-DOX at pH 7.4, at pH 5.5 and at pH 4 in PBS buffer at 37 °C.

PBS and acetate buffer solution (ABS) and found that the release of DOX is essentially nonexistent in a neutral environment (PBS, pH 7.4). In addition, this system exhibits a notable first burst release within 6 hours and almost completely releases after 48 hours in an acidic environment (ABS, pH 5.0).[48] This behavior can be explained by the possibility of DOX molecules being present on the outer surface of the particles rather than in their inner hollow cavity or core.

It is undoubtedly clear that the type of host material has a huge effect on the loading and release profiles. However, it is not just the material, but also how it is prepared that has an effect on the size, shape, BET surface area, and other factors that clearly subsequently affect the drug uptake and release too. The materials which we have prepared in our work have higher BET surface area values (446 m^2 g^{-1} for Y_2O_3:Er,Yb and 202 m^2 g^{-1} for $Y_2O_2SO_4$:Er,Yb precursor, respectively) compared to the above-discussed materials. They show very good DOX loading efficiencies (36.95% and 38.3%, respectively). Nevertheless, the slower DOX release relative to other materials can perhaps be explained by the fact that the loaded DOX diffuses from the pores of materials rather than its surface.[49]

This work therefore once again highlights possibilities of employing various hybrid and inorganic (nano)materials for biomedical thermometry purposes as well as the potential of simultaneously coupling thermometry with another modality for theranostic purposes as has already been shown for other similar materials in literature.[50–53]

Conclusions

In this work, we demonstrate how hollow Y_2O_3:Er,Yb and $Y_2O_2SO_4$:Er,Yb particles can be used as very sensitive thermometers in the physiological temperature range in an aqueous environment. We show that these materials can additionally be successfully loaded with the model anti-cancer drug DOX and the release can be controlled through pH change, which is appealing as cancer cells have lower pH values than healthy cells and tissue. We have also carried out preliminary cytotoxicity tests, indicating that these materials are mostly non-toxic to *in vitro* cultivated healthy human cells when used at moderate concentrations without further functionalization. To the best of our knowledge, these are the first inorganic hollow materials proposed for such dual-mode thermometry-drug release application.

Conflicts of interest

The authors declare no conflicts of interest.

Acknowledgements

This work is part of a project that has received funding from the European Research Council (ERC) under the European Union's Horizon 2020 research and innovation programme (Grant agreement No. 945945). A. M. K. additionally thanks Ghent University for BOF funding (BOF/STG/202002/004). A.G.S. acknowledges FWO (G043322N, I002620N) for support.

References

1 M. Dramicanin, *Luminescence thermometry: methods, materials, and applications*, Woodhead Publishing, 2018.

2 E. C. Ximendes, U. Rocha, T. O. Sales, N. Fernández, F. Sanz-Rodríguez, I. R. Martín, C. Jacinto and D. Jaque, *Adv. Funct. Mater.*, 2017, **27**, 1702249.

3 J. Zhou, B. Del Rosal, D. Jaque, S. Uchiyama and D. Jin, *Nat. Methods*, 2020, **17**, 967–980.

4 A. Bednarkiewicz, L. Marciniak, L. D. Carlos and D. Jaque, *Nanoscale*, 2020, **12**, 14405–14421.

5 X.-d. Wang, O. S. Wolfbeis and R. J. Meier, *Chem. Soc. Rev.*, 2013, **42**, 7834–7869.

6 D. Jaque and F. Vetrone, *Nanoscale*, 2012, **4**, 4301–4326.

7 D. Rosenblum, N. Joshi, W. Tao, J. M. Karp and D. Peer, *Nat. Commun.*, 2018, **9**, 1–12.

8 N. Degrauwe, A. Hocquelet, A. Digklia, N. Schaefer, A. Denys and R. Duran, *Front. Pharmacol.*, 2019, **10**, 450.

9 H. Suo, X. Zhao, Z. Zhang, Y. Wang, J. Sun, M. Jin and C. Guo, *Laser Photonics Rev.*, 2021, **15**, 2000319.

10 C. D. Brites, S. Balabhadra and L. D. Carlos, *Adv. Opt. Mater.*, 2019, **7**, 1801239.

11 M. Peng, A. M. Kaczmarek and K. Van Hecke, *ACS Appl. Mater. Interfaces*, 2022, **14**, 14367–14379.

12 J.-C. G. Bünzli and S. V. Eliseeva, *Chem. Sci.*, 2013, **4**, 1939–1949.

13 J. Liu, A. M. Kaczmarek and R. Van Deun, *Chem. Soc. Rev.*, 2018, **47**, 7225–7238.

14 C. Duan, L. Liang, L. Li, R. Zhang and Z. P. Xu, *J. Mater. Chem. B*, 2018, **6**, 192–209.

15 A. Bagheri, H. Arandiyan, C. Boyer and M. Lim, *Adv. Sci.*, 2016, **3**, 1500437.

16 K. Zhao, J. Sun, F. Wang, A. Song, K. Liu and H. Zhang, *ACS Appl. Bio Mater.*, 2020, **3**, 3975–3986.

17 E. Hemmer, P. Acosta-Mora, J. Mendez-Ramos and S. Fischer, *J. Mater. Chem. B*, 2017, **5**, 4365–4392.

18 X. Qin, J. Wang and Q. Yuan, *Front. Chem.*, 2020, **8**, 608578.

19 H. Chen, W. Zhang, G. Zhu, J. Xie and X. Chen, *Nat. Rev. Mater.*, 2017, **2**, 1–18.

20 X. Y. Wong, A. Sena-Torralba, R. Alvarez-Diduk, K. Muthoosamy and A. Merkoçi, *ACS Nano*, 2020, **14**, 2585–2627.

21 P. Zhao, Y. Zhu, X. Yang, K. Fan, J. Shen and C. Li, *RSC Adv.*, 2012, **2**, 10592–10597.

22 H. Terraschke, M. Franzreb and C. Wickleder, *Chem. - Eur. J.*, 2020, **26**, 6833–6838.

23 Y. Gao, Y. Qiu, X. Wang, Y. Bi, G. Zhao, F. Ding, Y. Sun and Z. Xu, *RSC Adv.*, 2018, **8**, 21857–21862.

24 F. Zhang, G. B. Braun, A. Pallaoro, Y. Zhang, Y. Shi, D. Cui, M. Moskovits, D. Zhao and G. D. Stucky, *Nano Lett.*, 2012, **12**, 61–67.

25 Y. Jia, T.-Y. Sun, J.-H. Wang, H. Huang, P. Li, X.-F. Yu and P. K. Chu, *CrystEngComm*, 2014, **16**, 6141–6148.

26 L. Zong, P. Xu, Y. Ding, K. Zhao, Z. Wang, X. Yan, R. Yu, J. Chen and X. Xing, *Small*, 2015, **11**, 2768–2773.

27 Y. Gao, H. Yu, C. Shi, G. Zhao, Y. Bi, B. Xu, F. Ding, Y. Sun and Z. Xu, *R. Soc. Open Sci.*, 2017, **4**, 171451.

28 D. Yang, G. Yang, X. Wang, R. Lv, S. Gai, F. He, A. Gulzar and P. Yang, *Nanoscale*, 2015, **7**, 12180–12191.

29 G. Chen, F. Chen, X. Liu, W. Ma, H. Luo, J. Li, R. Ma and G. Qiu, *Nano Res.*, 2014, **7**, 1093–1102.

30 V. M. Lojpur, P. S. Ahrenkiel and M. D. Dramićanin, *Nanoscale Res. Lett.*, 2013, **8**, 1–6.

31 F. Zhao, M. Yuan, W. Zhang and S. Gao, *J. Am. Chem. Soc.*, 2006, **128**, 11758–11759.

32 S.-L. Lin, Z.-R. Chen and C. A. Chang, *Nanotheranostics*, 2018, **2**, 243.

33 C. Larquet and S. Carenco, *Front. Chem.*, 2020, **8**, 179.

34 J. Zhu, L. Liao, X. Bian, J. Kong, P. Yang and B. Liu, *Small*, 2012, **8**, 2715–2720.

35 Y. Huang, E. Hemmer, F. Rosei and F. Vetrone, *J. Phys. Chem. B*, 2016, **120**, 4992–5001.

36 A. M. Kaczmarek, M. Suta, H. Rijckaert, A. Abalymov, I. Van Driessche, A. G. Skirtach, A. Meijerink and P. Van Der Voort, *Adv. Funct. Mater.*, 2020, **30**, 2003101.

37 A. M. Kaczmarek, Y. Y. Liu, M. K. Kaczmarek, H. Liu, F. Artizzu, L. D. Carlos and P. Van Der Voort, *Angew. Chem., Int. Ed.*, 2020, **59**, 1932–1940.

38 M. Suta and A. Meijerink, *Adv. Theory Simul.*, 2020, **3**, 2000176.

39 C. D. Brites, P. P. Lima, N. J. Silva, A. Millan, V. S. Amaral, F. Palacio and L. D. Carlos, *Nanoscale*, 2012, **4**, 4799–4829.

40 L. Jauffred, A. Samadi, H. Klingberg, P. M. Bendix and L. B. Oddershede, *Chem. Rev.*, 2019, **119**, 8087–8130.

41 H. Rijckaert, S. Premcheska, S. Mohanty, J. Verduijn, A. Skirtach and A. M. Kaczmarek, *Phys. B*, 2022, **626**, 413453.

42 M. Asadi, M. Ghahari, S. A. Hassanzadeh-Tabrizi, A. M. Arabi and R. Nasiri, *J. Chin. Chem. Soc.*, 2019, **67**, 720–731.

43 Y. Bai, Y. Li, R. Wang and Y. Li, *ACS Omega*, 2020, **5**, 5346–5355.

44 ISO 10993-5:2009, *Biological evaluation of medical devices—Part 5: Tests for in vitro cytotoxicity*, Canadian Standards Association, 2007, pp. 1–11.

45 K. M. Rao, S. Parambadath, A. Kumar, C.-S. Ha and S. S. Han, *ACS Biomater. Sci. Eng.*, 2018, **4**, 175–183.

46 Z. Yi, W. Lu, C. Qian, T. Zeng, L. Yin, H. Wang, L. Rao, H. Liu and S. Zeng, *Biomater. Sci.*, 2014, **2**, 1404–1411.

47 S. Huang, Z. Cheng, Y. Chen, B. Liu, X. Deng, P. a. Ma and J. Lin, *RSC Adv.*, 2015, **5**, 41985–41993.

48 K. Ge, C. Zhang, W. Sun, H. Liu, Y. Jin, Z. Li, X. J. Liang, G. Jia and J. Zhang, *ACS Appl. Mater. Interfaces*, 2016, **8**, 25078–25086.

49 W. Feng, X. Zhou, C. He, K. Qiu, W. Nie, L. Chen, H. Wang, X. Mo and Y. Zhang, *J. Mater. Chem. B*, 2013, **1**, 5886–5898.

50 J. You, G. Zhang and C. Li, *ACS Nano*, 2010, **4**(2), 1033–1041.

51 Z. Xu, P. Ma, C. Li, Z. Hou, X. Zhai, S. Huang and J. Lin, *Biomaterials*, 2011, **32**, 4161–4173.

52 S. Premcheska, M. Lederer and A. M. Kaczmarek, *Chem. Commun.*, 2022, **58**, 4288–4307.

53 H. Rijckaert, S. Mohanty, J. Verduijn, M. Lederer, B. Laforce, L. Vincze, A. Skirtach, K. Van Hecke and A. M. Kaczmarek, *J. Mater. Chem. C*, 2022, **10**, 10574–10585.